LLNL-JRNL-2012577

Lawrence Livermore National Laboratory

Enabling Accurate Chemical Modeling of Shocked Energetic Materials Using a Machine Learning Interatomic Potential

H Pham, N Goldman, T Bremer, L Fried, J Gaffney

March 2026

The Journal of Chemical Physics

Disclaimer

This work performed under the auspices of the U.S. Department of Energy by Lawrence Livermore National Laboratory under Contract DE-AC52-07NA27344.

Enabling Accurate Chemical Modeling of Shocked Energetic Materials Using a Machine Learning Interatomic Potential

Cong Huy Pham,[*,†] Nir Goldman,[†,‡] Laurence E. Fried,[†] Rebecca K. Lindsey,[¶,§] Jim A. Gaffney,[‖] and Peer-Timo Bremer[⊥]

†*Physical and Life Sciences Directorate, Lawrence Livermore National Laboratory, Livermore, California 94550, United States*

‡*Department of Chemical Engineering, University of California, Davis, California 95616, United States*

¶*Department of Chemical Engineering, University of Michigan, Ann Arbor, MI, 48109, USA*

§*Department of Materials Science and Engineering, University of Michigan, Ann Arbor, MI, 48109, USA*

‖*Lawrence Livermore National Laboratory, Livermore, California 94550, United States*

⊥*Computing Directorate, Lawrence Livermore National Laboratory, Livermore, California 94550, United States*

E-mail: pham20@llnl.gov

Abstract

Understanding the complex chemistry of organic materials under dynamic compression is important for many applications, but is challenging due to the large number of reactions occurring at various time scales. Here, we develop a machine learning potential based on Chebyshev polynomials to study the insensitive energetic material 1,3,5-triamino-2,4,6-trinitrobenzene (TATB) under detonation. We discuss a strategy for constructing diverse training data needed to capture the complex chemistry of TATB. Our potential demonstrates strong transferability across a wide range of thermodynamic conditions and other explosives, enabling accurate and reliable chemical modeling of organic materials under extreme conditions. The efficiency of our approach allows for simulations over several nanoseconds and for large system sizes, providing detailed insights into the chemistry of shocked TATB. The model accurately reproduces experimental Hugoniot equation of state data, and our simulations reveal the rapid formation of nitrogen-rich carbon clusters following shock. The methods and datasets developed here offer a robust framework for accurate chemical modeling of other shocked organic energetic materials.

1 Introduction

Understanding the chemical evolution of organic materials under dynamic compression is important in many fields such as aerospace, material science,[1–3] and astrochemistry.[4,5] The time to reach chemical equilibrium can vary from a few picoseconds[6,7] to several nanoseconds or even many microseconds,[8,9] depending on the decomposition of the material. Carbon-rich materials tend to have longer reaction times due to the slow process of carbon cluster nucleation and growth.[10] It is challenging to determine the reaction mechanisms using experimental methods because there are a huge number (hundreds or thousands) of elementary reactions across a wide range of time scales which usually occur under extreme conditions (1000s of K and 10s of GPa). Therefore, computational approaches such as molecular dynamics (MD) simulations can provide atomic-level detail of chemical reactions and help determine mechanisms for experimental observations.

In order to accurately capture the chemical reactivities of organic materials under shock compression, forces in MD simulations are often computed with highly accurate quantum mechanical methods, such as density functional theory (DFT), to simulate the breaking and forming processes of chemical bonds. While DFT calculations using standard generalized gradient approximation (GGA) are widely used, more accurate methods such as meta-GGA can result in significant improvements in accuracy for certain applications.[11,12] DFT-MD has been proven to yield good agreement with shock experiments for various materials like liquid nitrogen,[13] liquid water,[14,15] graphite-to-diamond transformation,[16] and cometary ices.[4] However, DFT-MD simulations are typically limited to picosecond time scales and nanometer system sizes. It is known that the reaction zone time and length of many common explosives are in the range of 10 ns to 100 ns and 60 nm to 800 nm, respectively,[9] which are well beyond the capability of DFT-MD simulations. During detonation, the highly exothermic decomposition of explosives releases carbon, which is known to form solid structures, including nanodiamonds.[1–3,17] This slow formation of carbon-rich soot particles can significantly influ-

ence the performance of high explosives (HEs). Despite this, the chemistry and evolution of carbon condensates have largely remained unknown for decades. MD simulations using density functional tight binding (DFTB),[18] a semi-empirical quantum mechanical method that is more computationally efficient than DFT, still do not reach the experimental time and length scales of chemical reactions in typical explosives. The time scale of shock simulations using DFTB-MD can be less than 0.5 ns for systems with only several hundred atoms.[10,19,20] Less computationally intensive methods, like the ReaxFF reactive force-field,[21–23] have been used to simulate organic explosives under shock waves, but they tend to overestimate shock temperature and pressure due to their low transferability under extreme conditions.[24,25] Therefore, there is a high demand for the development of accurate and efficient interatomic potentials for studying organic materials under dynamic compression.

Recently, machine learning interatomic potentials (MLIPs) have been proposed to achieve quantum mechanical level accuracy while maintaining computational efficiency similar to classical force-fields. After training on large datasets, MLIPs have the capability to simulate reactive chemistry in condensed phase systems, demonstrating good agreement with experimental data and/or high-accuracy reference data for a variety of systems with diverse chemical bond types.[26–29] There are significantly fewer studies focused on understanding the entire shock process of organic systems.[7,30,31] Under a shock wave, the system undergoes significant compression and the temperature rises rapidly. The challenge of such simulations lies in the requirement of good transferability of MLIPs across a wide range of thermodynamic conditions.

In previous works, the Chebyshev Interaction Model for Efficient Simulation (ChIMES),[32] a MLIP based on Chebyshev polynomial expansion, has been used to simulate relatively simple systems, such as liquid N_2[30] and liquid HN_3,[7] under shock waves and good agreement with experiments and/or DFT-MD simulations have been observed. Here, we expand the ChIMES framework to develop a MLIP for studying shocked 1,3,5-triamino-2,4,6-trinitrobenzene (TATB).

TATB ($C_6H_6N_6O_6$) is an insensitive carbon-rich explosives with an estimated reaction zone time in the microsecond regime.[9] Recovery experiments on detonated TATB indicated that the final products of detonation contain a mixture of carbon-rich amorphous solid clusters and small gas molecules.[33,34] Technically, the difficulty of developing a MLIP for TATB comes from the fact that TATB is a multi-element system, so there are many interaction types that need to be learned from accurate reference quantum mechanical data. The chemical reactivity of shocked TATB is complex with a huge number of reactions at different time scales. We present the general strategies for generating high-quality training data for complex TATB chemistry. The resulting ChIMES TATB model shows excellent transferability across various thermodynamic states, as well as other considered explosives: DNTF (3, 4-bis (3-nitrofurazan-4-yl) furoxan) and LLM-105 (2,6-diamino-3,5-dinitropyrazine 1-oxide) under extreme conditions. We applied the developed ChIMES model to simulate shocked TATB; we find that the Hugoniot equation of state is in excellent agreement with experiments. Early chemistry of shocked TATB shows the formation of nitrogen-rich carbon clusters. This contrasts with previous studies based on thermochemistry, where it was predicted that the chemistry of TATB is characterized by the formation of carbon in the diamond phase and the dissociation of N_2 to form atomic N.[35] The prediction of nitrogen-rich clusters is in agreement with recent recovery experiments, where it was found that recovered detonation soot from a TATB-based formulation has an N/C ratio of 0.25.[34]

2 Model generation

As discussed in previous work,[32,36] ChIMES utilizes a many-body expansion to compute the total energy of a system by considering clusters of atoms of varying sizes up to four atoms. Each many-body energy term is expressed using Chebyshev polynomial expansions, enabling a versatile description of energy changes with atomic positions. ChIMES coefficients are determined through fitting to reference data (energies, atomic forces, and stresses)

from quantum simulations, allowing for accurate descriptions of complex interactions in the system.

In this study, to improve the accuracy of the ChIMES model compared to previous work, all reference data used to fit ChIMES are computed at the level of the meta-GGA SCAN functional.[11,12] It was shown that SCAN can provide more accurate descriptions of structural and energetic properties for diverse systems than generalized gradient approximation (GGA) methods.[12,37,38] While SCAN is computationally more expensive than GGA, it is still less demanding than hybrid functionals,[39] providing a good balance between accuracy and efficiency for a wide range of applications.

2.1 Summary of training data

In order to study TATB under dynamic compression, our targeted ChIMES model should be able to maintain quantum accuracies for a wide range of relevant thermodynamic conditions. A summary of the training atomic configurations used, which consist of a diverse set of chemical and physical environments, is shown in Figure 1(a).

2.1.1 Nonreactive conditions

Experimental studies have shown that TATB molecular crystals remain stable under room temperature and pressures as high as 100 GPa.[40] To capture this behavior in simulation, solid TATB configurations at room temperature and varying pressures were included in the training data, ranging from low pressure (around 0 GPa with a density of 1.90 g/cm^3) to high pressure (approximately 50 GPa with a density of 3.19 g/cm^3). Additionally, incorporating liquid configurations of H_2O, NH_3, CH_4, and CO_2 under nonreactive conditions into the training dataset has proven effective in mitigating overfitting during model development.

Nanoscale shear bands have been found to significantly contribute to the chemical activation of shocked TATB by reducing reaction energy barriers.[41] To account for these effects, four atomic configurations sampled from amorphous TATB shear bands at varying densities,

as detailed in reference 41, were also incorporated into the initial training dataset.

2.1.2 Reactive conditions

A critical component of the training data includes TATB configurations under dissociation conditions. Previous shock simulations have demonstrated that the density of shocked TATB can reach values as high as 3.5-4 g/cm^3 at shock velocities of 9–10 km/s.[10] To accurately model shocked TATB at shock velocities up to 10 km/s, configurations at elevated densities and temperatures were incorporated into the training dataset. The selected thermodynamic conditions were (T, ρ) values of (2000 K, 2.37 g/cm^3), (4000 K, 3.47 g/cm^3), and (5000 K, 3.97 g/cm^3).

Generating a comprehensive training dataset for TATB is challenging due to its complex structure, which involves four distinct element types. To avoid overfitting, it is crucial to individually capture the interactions between each atom pair. As part of the training data, liquid or amorphous structures for various systems with stoichiometric ratios of X/Y = 1/1, X/Y = 1/3, and X/Y = 3/1 were included, where X and Y represent the elements C, H, N, or O. Initial configurations for these structures were generated by randomly placing the atoms in a cubic cell of 12 Å, followed by structure optimization and then NVT simulation at 3000 K using DFTB (see section 8).

2.1.3 Gas phase configurations

The main objective of developing the ChIMES potential for TATB in this work is to explore condensed-phase chemistry. However, including gas-phase configurations is crucial to enhance the stability of the resulting potential, as discussed in previous work.[7,42] In the condensed system, there are abundant data for atomic forces for each frame, but only a single total energy value is used, which could result in inaccuracies in the relative energies between reactants and products. This challenge can be overcome by adding forces and energies for isolated species to the training set.

In previous work,[43] we demonstrated that using Δ-learning approach within a DFTB/ChIMES model requires only a small fraction of the training data (approximately 0.3% or ∼ 14k molecular geometries) to achieve a similar accuracy, compared to a neural network potential trained on 5M molecular conformations.[44] Here, the energies and atomic forces of ∼ 14k representative molecular configurations from the ANI-1x dataset were re-evaluated using the SCAN meta-GGA functional in a spin-polarized calculation (ISPIN=2 in VASP) and incorporated into the training data.

2.2 Iterative learning scheme

As in previous ChIMES studies,[7,32,42,45] we employ an iterative fitting scheme to improve the stability of the ChIMES potential. The specific details of the scheme applied to TATB are illustrated in Figure 1(b).

The initial training data for TATB includes molecular crystal TATB at room temperature with two distinct densities (1.90 and 3.19 g/cm^3), TATB configurations, liquid TATB under dissociation conditions (2000 K and 2.37 g/cm^3), and a set of gas-phase molecules taken from reference 43. Conducting direct DFT-MD simulations using the SCAN functional for TATB would be computationally prohibitive. Therefore, TATB configurations at both ambient and extreme conditions were obtained from MD simulations performed using DFTB. The shear band TATB and gas molecule configurations are taken directly from reference 41 and 43, respectively. Subsequently, single-point DFT calculations using the SCAN functional were carried out to evaluate energies, atomic forces, and stresses.

Additionally, following the suggestion in reference 7, we generated random displacement structures from the condensed phase configurations by displacing each atom in all three Cartesian directions with a random magnitude between 0 and 0.1 Å. The inclusion of random displacement configurations can improve sampling in the short-range repulsive interactions and enhance the stability of the resulting potential.[7,32]

The initial ChIMES model was created by directly fitting to the original training data.

ChIMES-NVT simulations were performed across various systems, including different solid and liquid TATB configurations as well as other liquids, under varying densities and temperatures at both ambient and extreme conditions (see Figure 1(b) and Table 1). Atomic configurations from the MD trajectories were periodically sent to DFT for single-point evaluations, which were then combined with the existing training set. A new ChIMES model was subsequently generated, and this iterative process continued until all NVT simulations using ChIMES across a broad range of systems and thermodynamic conditions were stable. Further details about the ChIMES functional form, the fitting procedure can be found in the Supporting Information.

2.3 Group cross validation

In order to avoid over-parametrization we use a k-fold group cross validation technique to test the predictive capability of the TATB potential model. In k-fold cross-validation the data set is divided into training and validation sub-sets, called folds, such that each data entry appears exactly once in a validation fold.[46] K-fold cross validation is simple to implement and has the advantage of using all data in validating one of the folds. We chose 10 folds, which is a common choice that uses roughly 90% of the data in training and 10% in validation for each fold.[46] One weakness of k-fold cross-validation is that data used in training may be highly correlated with data used in validation. This problem, called "data leakage" occurs when data entries are highly correlated with one another. Time series data, such as configurations from a molecular dynamics simulation, are often highly correlated. When data leakage occurs cross-validation can provide overly optimistic assessments of the models' predictive capabilities.[46]

In order to overcome this issue, we have employed a technique called group (or blocked) cross-validation.[46] In group cross validation correlated data entries are collected into groups, and entire groups are placed either in the training or validation set of each fold. This prevents the correlated data from appearing in both the training and validation set of any

fold. In our implementation we chose a group to be configurations sampled from a condensed phase trajectory or the configurations of a particular gas phase molecule. Gas phase groups consisted of configurations from 1,113 gas phase molecules, with 0 to 14 C atoms, 0 to 9 N atoms, 0 to 9 O atoms, and 0 to 32 H atoms. The condensed phase training data consisted of samples from 54 trajectories. Of these 54 trajectories, 18 were simulations of TATB under either reactive or non-reactive conditions. The remaining 36 trajectories were of other molecular systems as given in Table 1.

In our first attempt to perform group cross validation, we found a high variance between folds, where 2 of the 10 folds showed very high fitting errors even when a relatively small (less than 1000) number of parameters was used. We interpreted this to indictate that some groups were essential to obtain reasonable fits. A possible solution to this problem would be to add additional training data so that there would be more redundancy between the groups. Given limited computational resources, however, we decided to exclude a small number of groups from the validation sets for all folds. The groups excluded from validation included three gas phase molecules (CO, H_8O_6, and N_2O.) This was a very small fraction of the 1,113 gas phase molecules used in the training set. The condensed phase trajectories excluded from validation were two trajectories with random displacements of TATB, CN at pressures between 50 and 90 GPa, H_3N, N_3O, and HO_3. Thus, a total of 6 condensed phase trajectories were excluded from validation, with the other 48 condensed phase trajactories used in one of the validation folds.

We used the Least Absolute Shrinkage and Selection Operator (LASSO)[47] to regularize the parameters. LASSO regularizes the regression problem by setting certain parameters to 0. The number of parameters set to 0 is controlled by a user-defined regularization parameter. We used a locally developed parallel implementation of the LARS (Least Angle Regression)[48] algorithm for finding solutions to LASSO regularization. The LARS algorithm adds or removes parameters one at a time at a relatively low computational cost. One advantage of the LARS approach is that an entire set of solutions to the regression problem is generated

for each possible number of nonzero parameters. We defined an objective function $F_{\rm obj}$ to be:

$$F_{\rm obj} = \left[\frac{1}{D}\sum_{i=1}^{N_f}\sum_{j=1}^{N_a(i)}\sum_{k=1}^{3}(F_{i,j,k}^{\rm SCAN}-F_{i,j,k}^{\rm ChIMES})^2 + w_E^2(E_i^{\rm SCAN}-E_i^{\rm ChIMES})^2 + w_S^2\sum_{j=1}^{3}\sum_{k<j}(\sigma_{ijk}^{\rm SCAN}-\sigma_{ijk}^{\rm ChIMES})^2\right]^{1/2} \quad (1)$$

Here, N_f is the total number of configurations (frames) in the set. $N_a(i)$ is the number of atoms in the ith frame. $F_{i,j,k}$ is the kth component of the force on atom j in frame i, given in units of kcal/mol-Å. E_i is the energy per atom of the ith frame in units of kcal/mol. σ_{ijk}, is the (j,k)th component of the stress tensor of frame i in units of kcal/mol-Å^3. Stress tensors are not computed for gas phase configurations. w_E and w_S are weight factors for energies and stresses, respectively. In this work, we used $w_E = 200/\text{Å}$ and $w_S = 500/\text{Å}^2$. D is the total number of data entries.

In Figure 2(a) we show the regression objective function vs. the number of fitting parameters for each of the folds for the training data. The error metric for each fold behaves similarly as a function of the number of parameters. During training additional parameters always lead to a steady decrease in the error metric. In Figure 2(b) we show the corresponding plot for the validation data. There is a significant difference between each fold. Above 2000 parameters, there is a very slow decrease in the error metric averaged across folds, while for the training data a much larger decrease in the average error metric is found. This suggests that using roughly 2000 parameters is a conservative choice for the number of non-zero parameters in the model. In the final TATB model used for simulations 2300 parameters were used, and all data were used to train the model. The ChIMES model for TATB has a total of 13,808 possible non-zero parameters, so the use of LASSO regularization leads to significant computational savings in evaluating the potential when compared to a regularization technique such as ridge regression,[49] which would have determined non-zero

values for all 13,808 parameters.

In Figure 3 we compare DFT force xyz components vs. ChIMES force components from all of the validation sets in the 10 folds. A hexagonally binned histogram (hexbin) plot is shown. In this plot, the X-Y plane is divided into hexagonal bins. The count of the number of validation data points (using all cross-validation folds) in each bin is calculated. The resulting data count value is shown in the corresponding X-Y location, with a color given in the map. Please note the use of a logarithmic scale in the color map, which clearly displays rare outliers. Forces are consistently predicted in the validation sets, with similar errors (deviations from the line $y = x$) for the elements H, C, N, and O.

In Figure 4 we compare DFT stress components and energies vs. ChIMES. Diagonal stresses are centered on the $y = x$ line, but off-diagonal stresses are not well predicted by the TATB model. Those stress components are significantly less than the diagonal components, and are similar in magnitude to the error in the diagonal stresses. Energies are very well predicted in the validation sets, with the level curves tightly centered around $y = x$. This is likely due to the relatively high weight placed on energies in the fitting process. We have found that a high accuracy in energy helps to produce a stable ChIMES model, by ensuring that trajectories avoid unphysical configurations. We also note that, in this case, the error in the force predictions is larger than in the energy predictions, and for a substantial number of force data points ChIMES predicts forces with the opposite sign compared to DFT (see Figure 3). Reducing the energy weight or increasing the ChIMES model complexity could potentially reduce the force prediction errors and is the subject of ongoing work.

3 ChIMES performance for carbon allotropes and TATB under nonreactive conditions

Figure 5(a) shows the experimental pressure-volume data, along with computed results obtained using the SCAN functional and the ChIMES potential. The experimental data are

taken from Efthimiopoulos *et al.*[50] and Occelli *et al.*[51] In all cases, ChIMES closely reproduces the results of the SCAN-DFT reference method, and both show excellent agreement with experimental measurements. These findings demonstrate that the ChIMES potential developed here can accurately describe the structural properties of solid carbon, which is important for understanding carbon condensation phenomena during the shock detonation of explosives.[1–3,17]

A comparison between the experimental pressure-volume data and the calculated values using ChIMES potential and SCAN functional for nonreactive TATB is presented in Figure 5(b). Experimental data are taken from Stevens *et al.*,[52] Stavrou *et al.*,[53] and Plisson *et al.*[54] and they agree very well with each other in the low-pressure regime of less than 20 GPa. In this pressure range, DFT and ChIMES accurately predict the equilibrium volume as a function of pressure with deviations within the range of experimental uncertainty. At pressures above 20 GPa, the computed equilibrium volumes using ChIMES are in better agreement with the DFT values than experiment. In this pressure range, only experimental data from Plisson *et al.*[54] are available, and both ChIMES and DFT underestimate the equilibrium volume by $\sim 4\%$. It is worth noting that adding a dispersion correction to DFT could further improve agreement with experiments, as suggested in reference 54. However, the purpose of the comparison here is to show that ChIMES can reproduce DFT predictions (at the level of the reference method) for the nonreactive equation of state of TATB only. A recent nonreactive force-field has been developed to accurately describe a number of properties of single crystal and gas phase TATB.[55]

4 ChIMES performance for TATB at reactive conditions

To test the ChIMES performance for TATB at extreme conditions, we compare ChIMES and DFT for the structural properties and chemistry of liquid TATB at 3.0 g/cm^3 and 3000 K. The radial distribution functions (RDFs) for C-C and N-N are shown in Figure 6(a) and

Figure 6(b) to compare the structural properties predicted by ChIMES against DFT. We observe that the first peak of both C-C and N-N RDFs of the ChIMES model are slightly over-structured compared to DFT predictions. Interestingly, both ChIMES and DFT predict a bimodal N-N RDF at 1.1 Å and 1.3 Å, corresponding to N_2 molecules and N-N bonds in CN-containing rings. Overall, ChIMES predicts structural properties in good agreement with DFT results. The RDFs for other atom pairs also demonstrate good agreement between ChIMES and DFT, as shown in Figure S1 in the Supplementary Materials. The chemistry for dominant products predicted by ChIMES and DFT is shown in Fig.6(c) for mole fractions and Fig.6(d) for lifetimes. We employed an in-house code to determine the concentrations and lifetimes of the chemical products, where a group of atoms is identified as a molecule if it stays within a prescribed set of distance cutoffs for a specified minimum duration. The cutoff distance for each atom pair is chosen as the position of the first minimum in the corresponding pair RDF. The minimum bond lifetime is set to 30 fs, which is a typical value for hydrogen containing bonds under extreme conditions.[56] Although the resulting mole fractions and lifetimes of the chemical products can vary with the choice of cutoff distances and minimum bond lifetime, our objective here is simply to enable a consistent comparison of the chemistry predicted by ChIMES and DFT. We also note that the uncertainties associated with species identification can be significant, due to the relatively short length of the DFT-MD trajectories. In all cases, the products are dominated by N_2 molecules, which exhibit significantly higher mole fractions and lifetimes than other species. Our ChIMES model shows excellent agreement with DFT, with discrepancies below 5% for both mole fraction and lifetime. The computed molecular lifetimes are also within the range of reported values for other organic systems at extreme conditions.[7,56]

We note that the thermodynamic condition chosen here is not in the training data. So the agreement between ChIMES and DFT demonstrates the good transferability of our ChIMES model to pressure-temperature conditions that are outside the training data. This is crucial for studying shocked TATB across a wide range of thermodynamic states, from ambient (0

GPa and 298 K) to extreme conditions (100s of GPa and 1000s of K).

5 Hugoniot equation of state of TATB from shock simulations

In this section, we apply the presently developed ChIMES force field to study shock-driven detonation of the molecular crystal TATB through extended-Lagrangian molecular dynamics simulations using the multi-scale shock technique (MSST)[57,58] in LAMMPS.[59] MSST is a MD based method that simulates steady shock waves by constraining the stress and energy of the system according to the Rayleigh line and the Hugoniot energy relations. This approach enables shock simulations to be performed using significantly fewer atoms, drastically reducing computational effort compared to direct-shock simulations, which often require millions of atoms. MSST has been successfully employed to accurately reproduce the shock Hugoniot for various systems.[4,10,13,16,31]

The primary unit-cell of the molecular crystal TATB is prepared in an orthogonal computational cell with initial parameters $a = 18.04$ Å, $b = 15.27$ Å, and $c = 37.36$ Å, periodic boundary conditions, and a total of 48 molecules. The simulated shock-wave travels in the $z-$ direction, and computational cell mass-like parameter and macroscopic explicit viscosity were set to $Q = 10^{-15}\text{kg}^2/\text{m}^4$ and $\mu = 10^{-2}\text{kg/m/s}$, respectively. We use a small timestep of 0.1 fs to ensure accurate integration of the equations of motion in our MD simulations. The systems are first equilibrated in the NVT ensemble for 20 ps, followed by MSST simulations. Further details of the MSST and NVT simulations using ChIMES are provided in the LAMMPS input files in the Supporting Information. It is important to note that due to the significantly higher computational efficiency of ChIMES, the system size and simulation time here are 1152 atoms and 2 ns, which are much larger and longer than the ones using DFTB in reference 10, where the simulation contains a maximum of 192 atoms and the simulation time is less than 0.5 ns.

Figure 7 shows the time evolution of temperature (a) and density (b) for shock waves that propagate along lattice vector c at various shock velocities for 2 ns of the MSST simulations. The selected shock speeds (8.5, 9, and 10 km/s) are above the reported detonation velocity of 7.76 km/s of TATB.[60] As can be seen in Figure 7(a), the temperatures of the systems increase over time as chemistry occurs and reach equilibrium values with different time scales, depending on the shock strength. This temperature equilibration time ranges from about 20 ps to up to 200 ps for the strongest and weakest shock strength in this study respectively, corresponding to shock speeds of 10 km/s and 8.5 km/s, respectively. During the thermodynamic equilibration time, the system is rapidly compressed and then slowly expands before reaching equilibrium (see Figure 7(b)). The computed TATB Hugoniot data using ChIMES are plotted in Figure 7(c) and (d), together with experimental data from references 61 and 62. The deviation between the measured data in these two experiments is due to differences in the systems studied. Marshall *et al.* measured the Hugoniot data for single crystal TATB,[61] while Sollier *et al.* used a formulation containing 97/3 wt.% TATB/plastic. Importantly, our simulated Hugoniot data exhibit excellent agreement with the experimental results of Marshall *et al.*, demonstrating the robustness and accuracy of the ChIMES model in capturing the shock response of reacting TATB.

To investigate the structural changes in TATB under shock detonation, Figure 8(a) plots the time evolution of bond counts for C-C and C-N bonds. In the analysis two atoms form a bond if their distance is smaller than 1.6 Å. As time progresses, the number of C-C bonds decreases, followed by an increase in the number of C-N bonds, indicating the formation of nitrogen-rich carbon clusters. This is in agreement with the previous study using DFTB.[10] The time taken to reach equilibration in the bond counts depends on the shock strength and the bond type. With a shock speed of 8.5 km/s, the number of C-C bonds change slightly after about 200 ps, while C-N bonds take more time, as significantly more bonds are forming in the range of 200-500 ps. A higher shock speed accelerates reactions, as seen in the case of a shock speed of 10 km/s, where both the number of C-C and C-N bonds show small variations

after 50 ps. Figure 8(b) shows an example of the cluster forming during the simulation. No carbon condensation was observed in all MSST simulations with the current system size up to 2 ns in this study. Here, we observe that the cluster spanning the simulation cell forms rapidly during the shock simulations, with a stable composition of 0.28 C, 0.23 H, 0.28 N, and 0.21 O. This differs from other MD simulations, such as Manaa *et al.*,[10] which reported a composition of 0.58 C, 0.34 N, and 0.08 O using a self-consistent charge density-functional tight binding method, and Zhang *et al.*,[63] which obtained 0.47 C, 0.15 H, 0.08 N, and 0.31 O using a ReaxFF reactive force field. A very recent study by Bidault et al.[23] found a condensed foam with an elemental composition at the C-J state of roughly (0.44 C, 0.13 H, 0.08 N, 0.35 O). Molecular dynamics methods agree that a condensate is rapidly formed in shocked TATB, but the elemental composition of the condensate is sensitive to the method used to calculate the interatomic potential energy. It is important to note that the MD model in this study is fitted to a higher-accuracy method, and the simulation time is significantly longer than that of Manaa et al. (2 ns versus 500 ps). Recent recovery experiments have measured the chemical decomposition of the detonation soot as 0.596 C, 0.149 N, and 0.255 O.[34] Our clusters are richer in O, N, and H than recovery experiments show. It is likely that the chemical composition of the clusters evolve as the system expands and cools during the detonation process. This will be the subject of further study.

We evaluated the accuracy of the ChIMES model in predicting energies, atomic forces, and stresses for configurations sampled during the dynamic shock process. A set of 30 configurations, evenly spaced along the MD trajectory from the MSST simulations, was selected for single-point energy evaluations using both ChIMES and DFT with the SCAN functional. The comparison between ChIMES and DFT results is presented in Figure S2. Overall, ChIMES demonstrates high accuracy in predicting energies, atomic forces, and stresses, with RMSE values within the error range of the fit to the training data. The strong agreement between the ChIMES model predictions and DFT calculations confirms that ChIMES effectively captures the complex atomic interactions in TATB during dynamic

compression.

We further evaluated the chemistry predictions of a ChIMES model trained to a subset of the data as described in Section 2.3 for TATB under shock wave conditions. The model exhibits the same behavior in the time evolution of C-C and C-N bond counts (see Figure S3 in the Supporting Information). Notably, the formation of nitrogen-rich carbon clusters, as indicated by the increasing number of C-N bonds, is consistently observed and verified using this independent ChIMES model. This consistency between the ChIMES predictions further strengthens the reliability and robustness of the ChIMES models in accurately capturing cluster formation dynamics under shock conditions.

It is worth mentioning that the timescale for chemical equilibration in shocked TATB can be up to several microseconds due to slow carbon condensation. To simulate this process, we would need access to a system size and time scale much larger and longer than the ones used in this study. A detailed analysis would require systematic studies of chemistry and how the carbon clusters form as a function of system size, similar to the studies in references 45 and 64, and it is the subject of ongoing work.

6 Transferability of ChIMES TATB model to DNTF and LLM-105

Next, we evaluate the performance of the ChIMES TATB model on other explosives that are not part of the training data. We selected molecular crystals of DNTF and LLM-105 since DFT-MD simulations for these systems are available.[20,65] We compare the ability to predict average pressure in NVT simulations between ChIMES and the recently developed ANI-1xnr[29] and MACE-MP-0[66] potentials against DFT data. ANI-1xnr is a reactive potential designed for modeling reactions in condensed phase organic systems. By training on a diverse dataset, ANI-1xnr potential is transferable to a wide range of reactive materials.[29] The MACE-MP-0 model was developed for stable MD simulations of molecules and inor-

ganic materials, with training data includes public database of 150k crystal structures. It has been shown that MACE-MP-0 can be used to study a variety of problems, including chemical reactions in organic materials.[66] The comparison in Figure 9(a) shows that ChIMES, ANI-1xnr, and MACE-MP-0 provide good agreement with DFT data over a wide range of pressure and density for DNTF. ChIMES and MACE-MP-0 demonstrates higher accuracy than ANI-1xnr at higher temperatures and densities. The largest deviation from DFT in pressure prediction of ANI-1xnr is about 10 GPa at $(\mathrm{T}, \rho) = (4700\ \mathrm{K},\ 2.8\ \mathrm{g/cm^3})$, while the deviations for MACE-MP-0 and ChIMES are 3.2 and 3.0 GPa, respectively. Additionally, ChIMES outperforms ANI-1xnr and MACE-MP-0 in the case of LLM-105, particularly at high-density states, as shown in Figure 9(b). In some cases, the pressure values predicted by ANI-1xnr and MACE-MP-0 differ from DFT values by ∼15-20 GPa while the maximum deviation of ChIMES predictions from DFT values is only about 5 GPa.

It is important to note that ChIMES, ANI-1xnr, and MACE-MP-0 are trained at the level of SCAN meta-GGA, BLYP-D3 GGA (Becke, Lee, Yang and Parr[67,68] with Grimme third-generation dispersion (D3) correction[69]), and PBE GGA, respectively; while DFT-MD is performed using PBE-D2 GGA (PBE functional with the D2 method for the description of dispersion interactions[70]). Of course, the difference in resulting pressure will vary with different DFT methods; however, quick single-point calculations using the three DFT functionals mentioned above on the same configurations from DFT-MD trajectories show a deviation of pressure values of less than 1 GPa. Therefore, we conclude that ChIMES gives a better prediction of pressure values than ANI-1xnr and MACE-MP-0 compared to DFT calculations. The result here also suggests that future developments of ANI-1xnr and MACE-MP-0 potentials for studying explosives under detonation require more training data at high pressure-temperature, as well as explosive compounds with common chemical groups, such as $-\mathrm{NO_2}$, $-\mathrm{ONO_2}$, and $-\mathrm{NHNO_2}$.

Since the reported DFT-MD trajectories for DNTF are very short (i.e. less than 2.5 ps), the system is still far from chemical equilibrium.[20] Therefore we do not compare the

performance of MLIPs for chemistry predictions. It was also shown that for the thermal decomposition of LLM-105 at various pressure temperature conditions, the ChIMES TATB model developed here provides good agreement with DFT-MD simulations and experiments,[65] demonstrating good transferability of our current ChIMES model for predicting chemical reactions of organic explosives. We also note that simulations of DNTF and LLM-105 at ambient conditions using the MLIPs in this study show some molecular dissociations, indicating the occurrence of chemical reactions. This suggests that directly applying the ChIMES model developed for TATB to other explosives under shock compression may not yield highly accurate results for the Hugoniot EOS or chemical reactivity. Further work is needed to develop ChIMES models with accuracy comparable to that achieved for TATB, specifically for other explosives such as LLM-105 and DNTF. This will be the focus of our future studies. These simulation efforts are critical for providing further insights into experimental observations of the differing detonation performance and shock insensitivity between insensitive HEs and conventional HEs.[71]

7 Conclusion

We have developed a ChIMES MLIP for studying complex chemistry of TATB under detonation reaction. By training on a diverse dataset at a highly accurate level of reference data (meta-GGA SCAN DFT), our ChIMES model shows good accuracy and transferability to other thermodynamic conditions and/or other organic explosives. We utilized the ChIMES MLIP to study shocked TATB and obtain good agreement with experimental data for the Hugoniot equation of state. Several ns long simulations show the formation of nitrogen-rich carbon clusters in the early chemistry of shocked TATB, in qualitative agreement with our previous study using DFTB.[10] In comparing with experimental results on recovered TATB detonation soots, we find higher amounts of impurity atoms than in experiment. This could be due to changes in the elemental composition of the clusters during the detonation pro-

cess. It could also be that the overdriven ($P > P_{\mathrm{CJ}}$) detonation conditions studied here yield differing condensate chemistries than the non-overdriven conditions of the experiment. The ChIMES model developed in this study can serve as a foundation model, with future development of ChIMES MLIP for other C, H, N, O-containing materials determined by refinement starting from the diverse training dataset developed in this study.

8 DFTB and DFT calculations

NVT simulations using DFTB were performed with self-consistent charges (SCC), using the DFTB+ package[72] with the 3ob-3-1 parameter set, which contains a third-order expansion about the charges and is considered an optimal DFTB starting point for most organic systems.[73] The SCC convergence criterion was set to 10^{-6} au and a time step of 0.1 fs was used. DFTB calculations in the canonical ensemble were performed with a Nose-Hoover thermostat. All NVT simulations using DFTB were run for about 5 ps, and training configurations were evenly spaced from the DFTB-MD trajectories.

All DFT simulations were performed using the VASP package[74–77] with a plane wave cutoff of 800 eV, projector-augmented wave (PAW) pseudopotentials.[78,79] Instead of using the Perdew-Burke-Ernzerhof (PBE) generalized gradient approximation functional,[80] as in previous works,[7,45] here we utilized a higher-level quantum calculations in the SCAN meta-generalized gradient approximation (meta-GGA)[11] that shows significant improvement in accuracy over the GGA functionals for a number of diversely bonded materials.[12] We also used spin-polarized calculations (ISPIN=2 in VASP) that would yield lowest energy states with the most stable spin configurations. This is important given the large number of open-shell systems in our training data.

9 Supplementary Material

See the supplementary material for: (I) ChIMES model generation for TATB (Sec. S1), (II) Comparison between DFT and ChIMES for RDFs of different atom pairs at extreme conditions (Fig. S1), (III) Comparison between DFT and ChIMES for energies, forces, and stress tensor predictions for 30 configurations sampled during the shock simulations (Fig. S2), (IV) Time evolution of C–C and C–N bond counts in shocked TATB, predicted by a ChIMES model trained to a subset of the group cross-validation data (Fig. S3), (V) Details of the LAMMPS installation and input files for MSST and NVT simulations.

Acknowledgement

This work was performed under the auspices of the U.S. Department of Energy by Lawrence Livermore National Laboratory under Contract DE-AC52-07NA27344 and was supported by the LLNL-LDRD Program under Project No. 24-SI-004. Simulations reported here were conducted by CHP. The cross-validation study was performed by LEF and CHP. LEF, JAG, and PTB contributed valuable discussion and insights. CHP, NG, and LEF wrote the manuscript. The manuscript was revised by all authors.

Table 1: Thermodynamic state points (density-temperature) of condensed configurations included in the training data. Atomic configurations are taken from NVT simulation at relevant density/pressure using density-functional tight-binding, followed by a single-point DFT calculation to re-evaluate the energy, forces and stresses. The value n_{int}/n_{fin} indicates the number of configurations in the initial/final training set. For states with $n_{ini} = 0$, the relevant structures were added using the iterative learning scheme only.

	ρ (g/cm^3)	T (K)	n_{ini}	n_{fin}
nonreactive conditions				
TATB molecular crystal	1.90	300	30	61
TATB molecular crystal	3.19	300	30	61
liquid $H_2O/NH_3/CH_4/CO_2$	1.00/0.74/0.45/1.18	300/270/100/250	0	31
TATB shearband	2.37/2.59/2.78/2.96	–	4	4
reactive conditions				
liquid TATB	2.37	2000	20	35
liquid TATB	3.47	4000	0	15
liquid TATB	3.97	5000	0	15
liquid/amorphous $C/H_2/N_2/O_2$	2.12/0.097/2.48/2.46	3000	0	23
X,Y=C,H/C,N/C,O/H,N/H,O/N,O				
liquid/amorphous XY	1.50/2.30/2.48/1.73/1.96/2.71	3000	0	23
liquid/amorphous XY_3	0.87/2.39/2.65/2.48/2.83/2.80	3000	0	23
liquid/amorphous X_3Y	2.13/2.21/2.30/0.98/1.10/2.62	3000	0	23

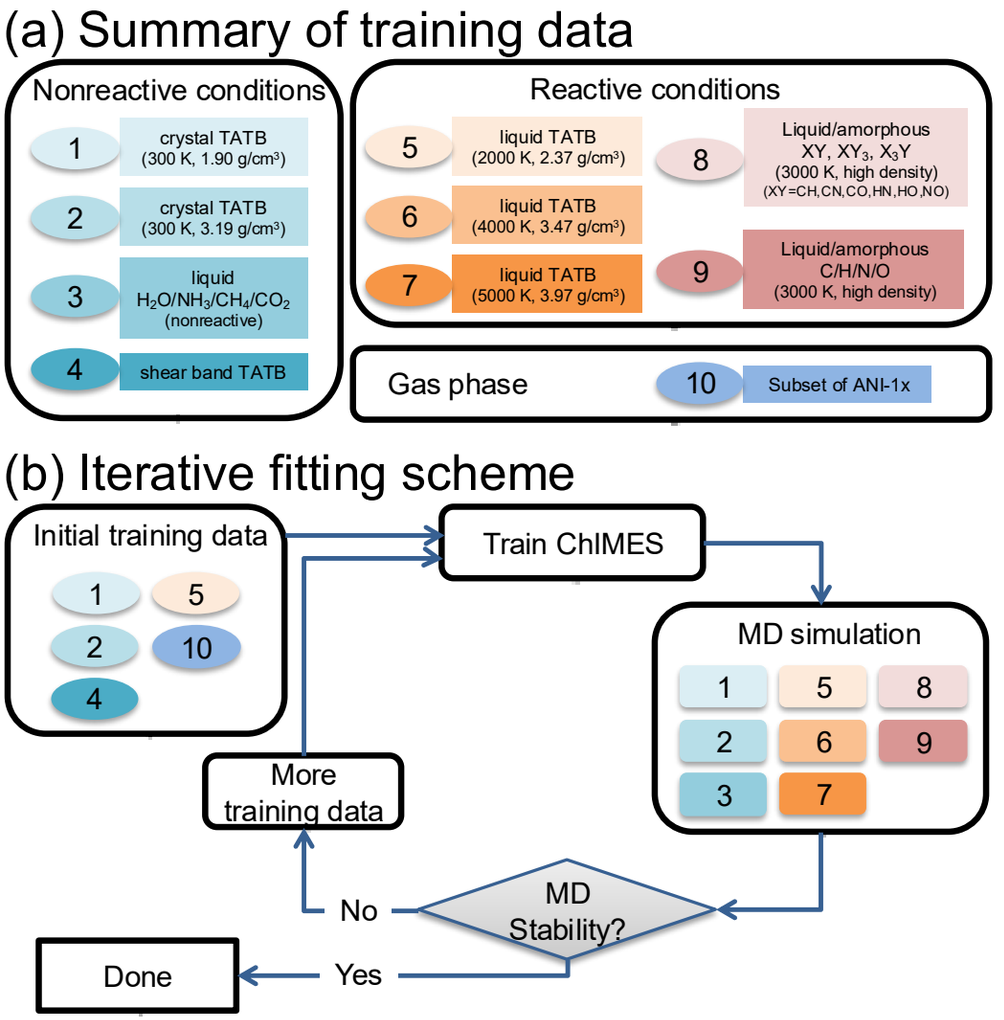

Figure 1: (a) A summary of training data with multiple types of configurations, (b) an iterative fitting scheme to generate a stable ChIMES model.

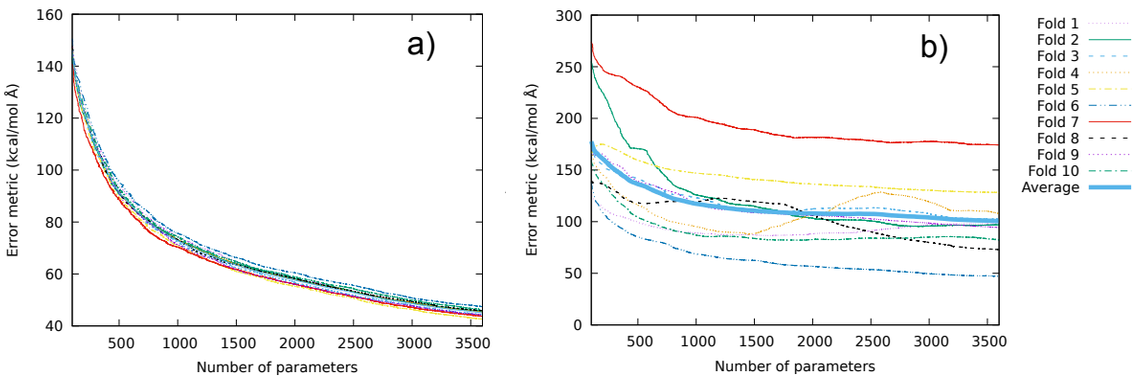

Figure 2: The fitting error metric is shown for training (a) and validation (b) data for each of the group cross-validation folds, along with the average value.

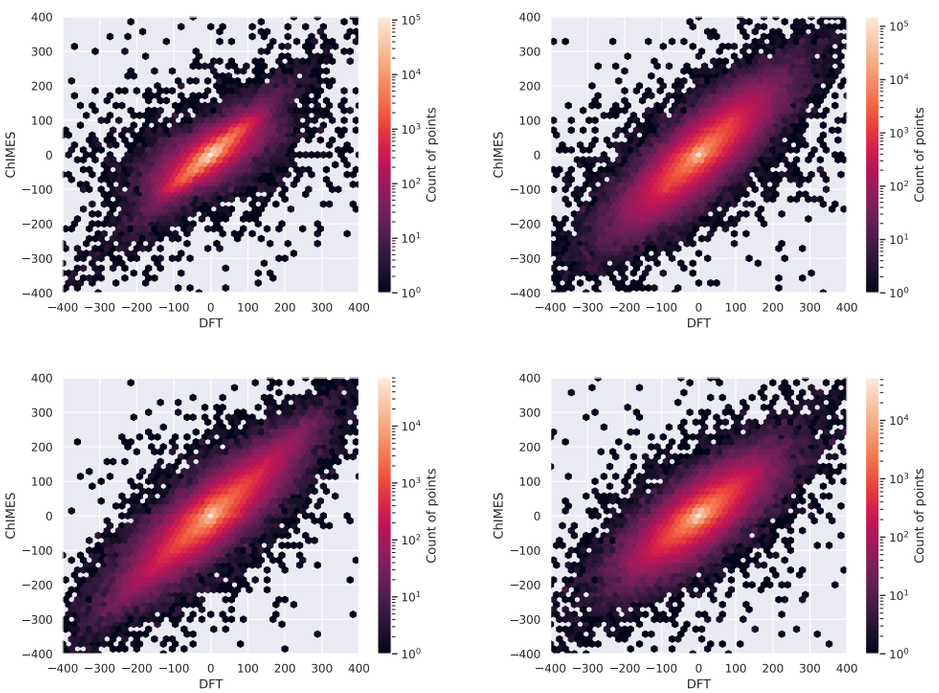

Figure 3: Hexagonally binned histograms of ChIMES validation set forces vs. DFT forces are shown for (a) H, (b) C, (c) N, (d) O atoms in units of kcal/mol-Å. Note the logarithmic color map.

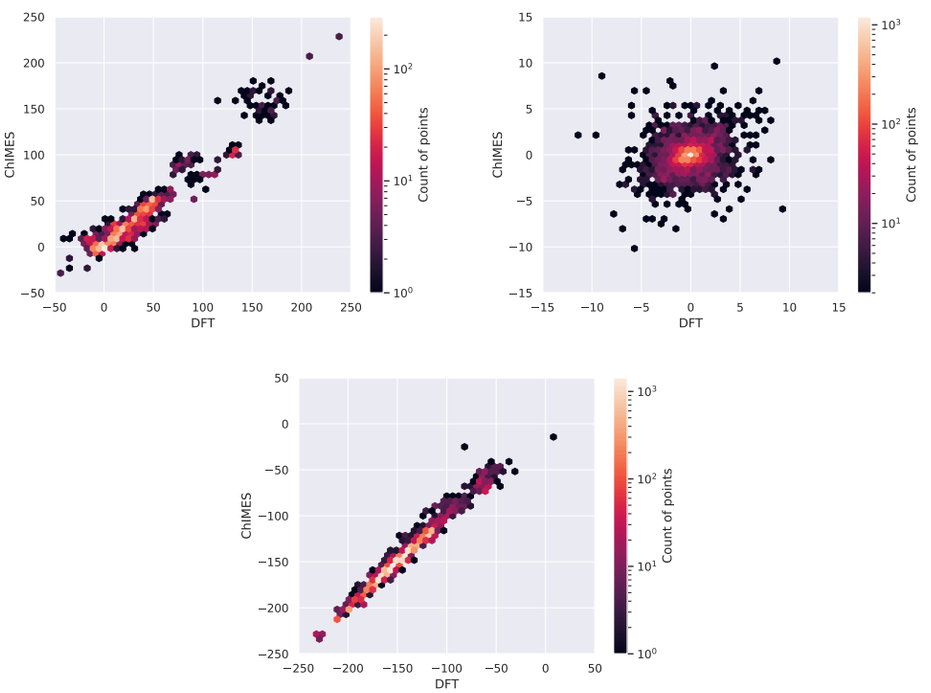

Figure 4: Hexagonally binned histograms of ChIMES validation set quantities vs. DFT quantities are shown for the quantities of (a) diagonal stress components, (b) off-diagonal stress components, (c) energy. Stress is shown in units of GPa, while energy is shown in units of kcal/mol. Note the logarithmic color map.

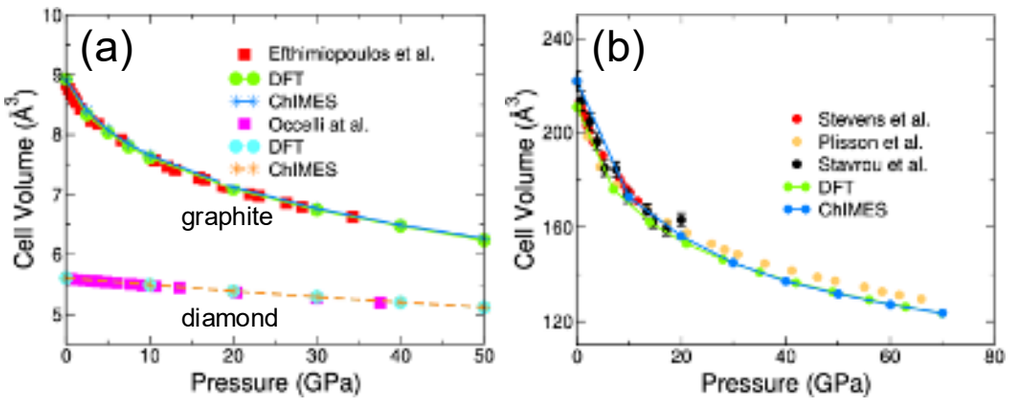

Figure 5: Comparison of experimental results, DFT calculations, and ChIMES predictions for the nonreacted equation of state of (a) graphite and diamond and (b) TATB. Experimental data for graphite are reproduced with permission from Efthimiopoulos et al., Phys. Rev. B 107, 184102 (2023). Copyright 2023 American Physical Society. Experimental data for diamond are reproduced with permission from Occelli et al., Nat. Mater. 2, 151–154 (2003). Copyright 2003 Springer Nature. Experimental data for TATB are reproduced with permission from Stevens et al., Propellants Explos. Pyrotech. 33, 286–295 (2008). Copyright 2008 Wiley-VCH GmbH. Experimental data for TATB are also reproduced from Stavrou et al., J. Appl. Phys. 119, 135904 (2016), and from Plisson et al., J. Appl. Phys. 122, 235901 (2017), with the permission of AIP Publishing.

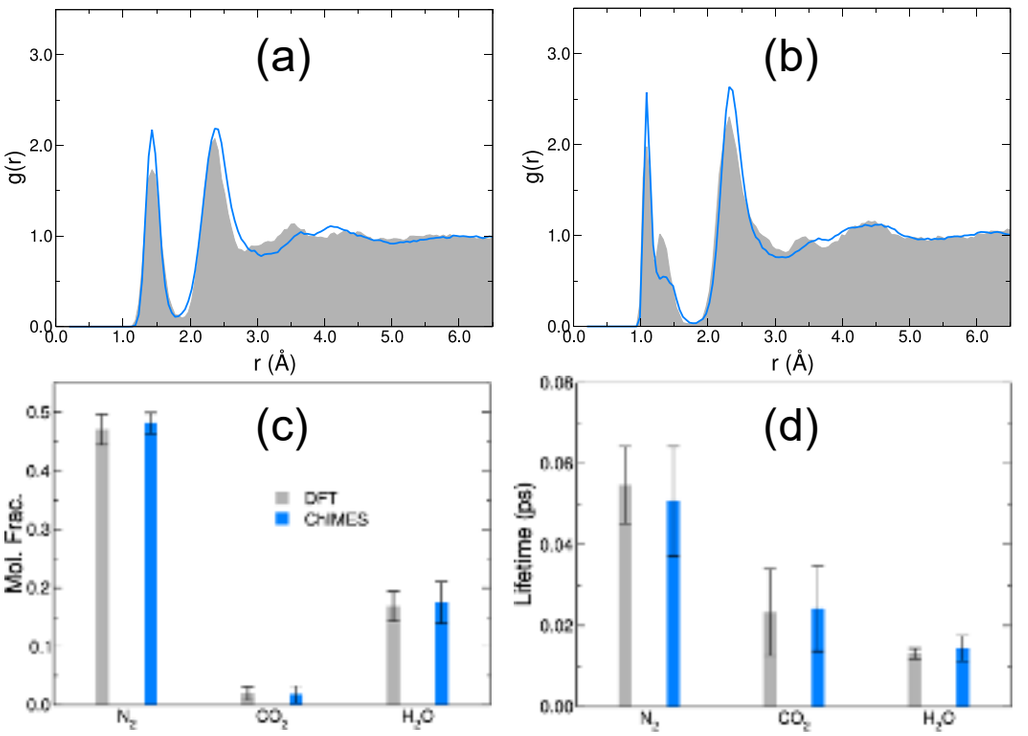

Figure 6: Predicted properties for TATB at 3.0 g/cm^3 and 3000 K by DFT (SCAN-metaGGA) and ChIMES model. Radial distribution functions for atom pairs C-C (a) and N-N (b). Small molecule speciation in liquid TATB predicted by DFT and ChIMES for mole fractions (c) and lifetimes (d).

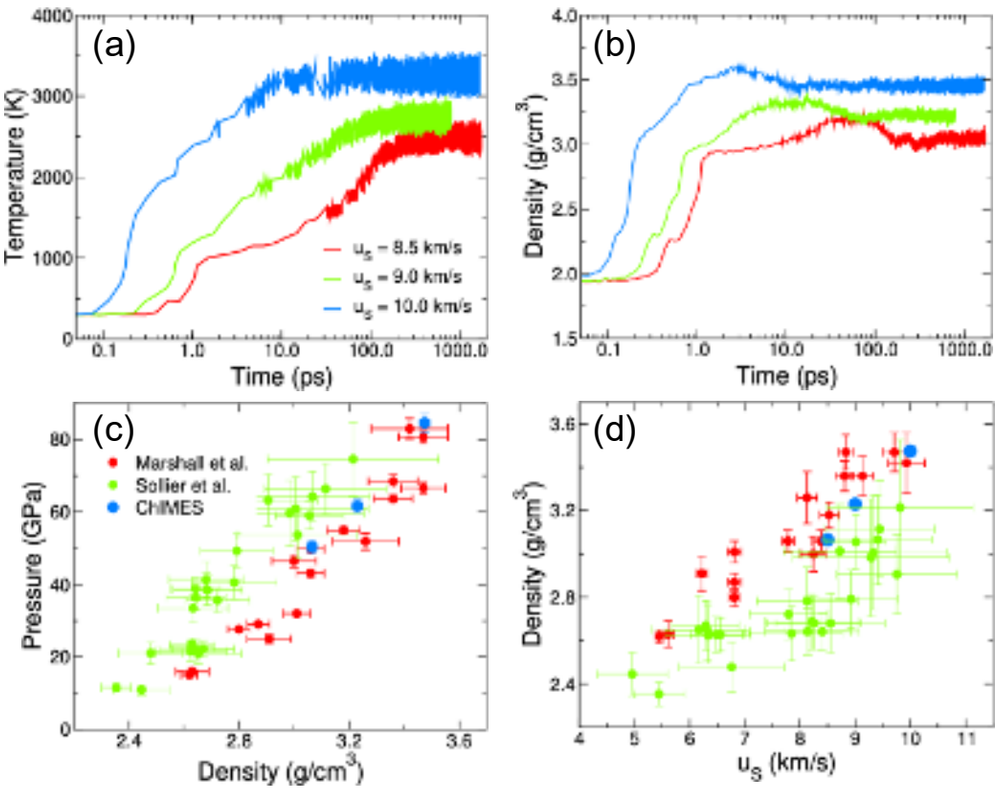

Figure 7: Time evolution of temperature (a) and density (b) for shocks of various speeds propagating through molecular crystal TATB from MSST simulations using the ChIMES potential. Computational TATB Hugoniot data from shock simulations are compared to experimental Hugoniot data reported in references 61,62. Shock pressure as a function of density (c) and density as a function of shock velocity (d). Experimental Hugoniot data for TATB are reproduced from Marshall et al., J. Appl. Phys. 127, 185901 (2020), and from Sollier et al., J. Appl. Phys. 135, 095901 (2024), with the permission of AIP Publishing.

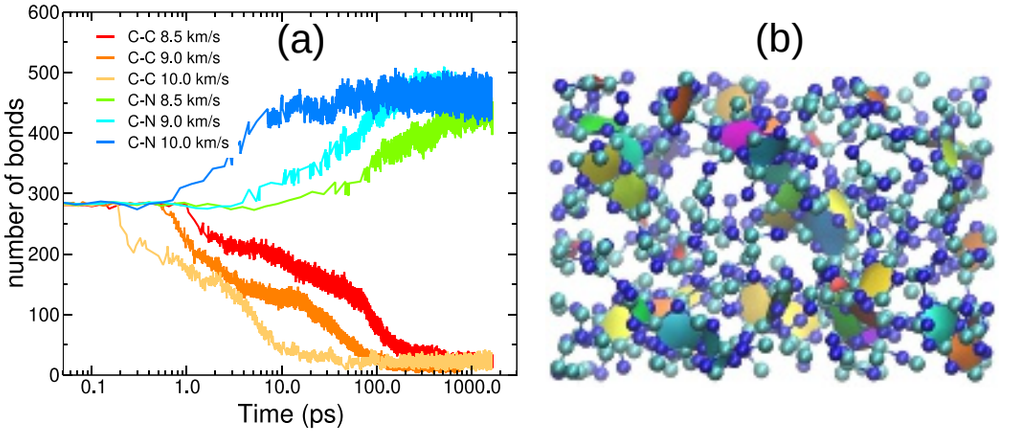

Figure 8: (a) Time evolution of bond counts for C-C and C-N in shocked TATB. (b) Representative nitrogen-rich carbon cluster after a 2 ns MD simulation of shocked TATB at a shock speed of 9 km/s. H and O atoms are removed for better visualization, C in cyan and N in blue.

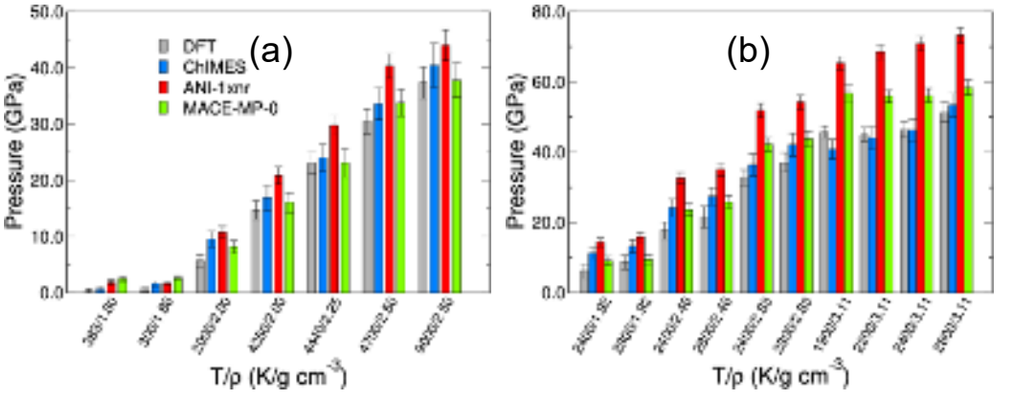

Figure 9: Average pressure from NVT simulations predicted by DFT, ChIMES, and ANI-1xnr at various thermodynamic states for DNTF (a) and LLM-105 (b).

References

(1) Greiner, N. R.; Phillips, D.; Johnson, J.; Volk, F. Diamonds in detonation soot. *Nature* **1988**, *333*, 440–442.

(2) Bagge-Hansen, M.; Bastea, S.; Hammons, J. A.; Nielsen, M. H.; Lauderbach, L. M.; Hodgin, R. L.; Pagoria, P.; May, C.; Aloni, S.; Jones, A.; Shaw, W. L.; Bukovsky, E. V.; Sinclair, N.; Gustavsen, R. L.; Watkins, E. B.; Jensen, B. J.; Dattelbaum, D. M.; Firestone, M. A.; Huber, R. C.; Ringstrand, B. S.; Lee, J. R.; van Buuren, T.; Fried, L. E.; Willey, T. M. Detonation synthesis of carbon nano-onions via liquid carbon condensation. *Nature Communications* **2019**, *10*, 1–8.

(3) Armstrong, M. R.; Lindsey, R. K.; Goldman, N.; Nielsen, M. H.; Stavrou, E.; Fried, L. E.; Zaug, J. M.; Bastea, S. Ultrafast shock synthesis of nanocarbon from a liquid precursor. *Nature Communications* **2020**, *11*, 353.

(4) Goldman, N.; Reed, E. J.; Fried, L. E.; William Kuo, I.-F.; Maiti, A. Synthesis of glycine-containing complexes in impacts of comets on early Earth. *Nature Chemistry* **2010**, *2*, 949–954.

(5) Martins, Z.; Price, M. C.; Goldman, N.; Sephton, M. A.; Burchell, M. J. Shock synthesis of amino acids from impacting cometary and icy planet surface analogues. *Nature Geoscience* **2013**, *6*, 1045–1049.

(6) Reed, E. J.; Rodriguez, A. W.; Manaa, M. R.; Fried, L. E.; Tarver, C. M. Ultrafast detonation of hydrazoic acid (HN 3). *Physical Review Letters* **2012**, *109*, 038301.

(7) Pham, C. H.; Lindsey, R. K.; Fried, L. E.; Goldman, N. Calculation of the detonation state of HN3 with quantum accuracy. *The Journal of Chemical Physics* **2020**, *153*, 224102.

(8) Mader, C. L. Numerical modeling of detonations. *Los Alamos Series in Basic and Applied Sciences (University of California Press)* **1979**,

(9) Tarver, C. M.; Tao, W. C.; Lee, C. G. Sideways Plate Push Test for Detonating Solid Explosives. *Propellants, Explosives, Pyrotechnics* **1996**, *21*, 238–246.

(10) Manaa, M. R.; Reed, E. J.; Fried, L. E.; Goldman, N. Nitrogen-rich heterocycles as reactivity retardants in shocked insensitive explosives. *Journal of the American Chemical Society* **2009**, *131*, 5483–5487.

(11) Sun, J.; Ruzsinszky, A.; Perdew, J. Strongly Constrained and Appropriately Normed Semilocal Density Functional. *Physical Review Letters* **2015**, *115*, 036402.

(12) Sun, J.; Remsing, R. C.; Zhang, Y.; Sun, Z.; Ruzsinszky, A.; Peng, H.; Yang, Z.; Paul, A.; Waghmare, U.; Wu, X.; Klein, M. L.; Perdew, J. P. Accurate first-principles structures and energies of diversely bonded systems from an efficient density functional. *Nature Chemistry* **2016**, *8*, 831–836.

(13) Kress, J. D.; Mazevet, S.; Collins, L. A.; Wood, W. W. Density-functional calculation of the Hugoniot of shocked liquid nitrogen. *Physical Review B* **2000**, *63*, 024203.

(14) Goldman, N.; Reed, E. J.; Kuo, I. F.; Fried, L. E.; Mundy, C. J.; Curioni, A. Ab initio simulation of the equation of state and kinetics of shocked water. *Journal of Chemical Physics* **2009**, *130*, 124517.

(15) Goldman, N.; Reed, E. J.; Fried, L. E. Quantum mechanical corrections to simulated shock Hugoniot temperatures. *Journal of Chemical Physics* **2009**, *131*, 204103.

(16) Mundy, C. J.; Curioni, A.; Goldman, N.; Kuo, I. F.; Reed, E. J.; Fried, L. E.; Ianuzzi, M. Ultrafast transformation of graphite to diamond: An ab initio study of graphite under shock compression. *Journal of Chemical Physics* **2008**, *128*, 184701.

(17) Bastea, S. Nanocarbon condensation in detonation. *Scientific Reports* **2017**, *7*, 1–6.

(18) Elstner, M.; Porezag, D.; Jungnickel, G.; Elsner, J.; Haugk, M.; Frauenheim, T. Self-consistent-charge density-functional tight-binding method for simulations of complex materials properties. *Physical Review B* **1998**, *58*, 7260.

(19) Reed, E. J.; Manaa, M. R.; Fried, L. E.; Glaesemann, K. R.; Joannopoulos, J. D. A transient semimetallic layer in detonating nitromethane. *Nature Physics* **2007**, *4*, 72–76.

(20) Lindsey, R. K.; Bastea, S.; Goldman, N.; Fried, L. E. Investigating 3,4-bis(3-nitrofurazan-4-yl)furoxan detonation with a rapidly tuned density functional tight binding model. *The Journal of Chemical Physics* **2021**, *154*, 164115.

(21) Duin, A. C. V.; Dasgupta, S.; Lorant, F.; Goddard, W. A. ReaxFF: A reactive force field for hydrocarbons. *Journal of Physical Chemistry A* **2001**, *105*, 9396–9409.

(22) Lafourcade, P.; Maillet, J.-B.; Roche, J.; Sakano, M.; Hamilton, B. W.; Strachan, A. Multiscale Reactive Model for 1,3,5-Triamino-2,4,6-trinitrobenzene Inferred by Reactive MD Simulations and Unsupervised Learning. *J. Phys. Chem. C* **2023**, *127*, 15556–15572.

(23) Bidault, X.; Lafourcade, P.; Dubois, V.; Maillet, J.-B. Carbon-rich foam formation in the early stages of detonation of 1,3,5-triamino-2,4,6-trinitrobenzene (TATB). *Journal of Chemical Physics* **2025**, *163*, 144305.

(24) Jiang, J.; Liu, J.; Chen, Y.; Wu, Q.; Ju, Z.; Zhang, S. Detonation response mechanism of shocked LLM-105 using ReaxFF-lg and MSST. *Molecular Simulation* **2021**, *47*, 678–687.

(25) Hamilton, B. W.; Kroonblawd, M. P.; Islam, M. M.; Strachan, A. Sensitivity of the Shock Initiation Threshold of 1,3,5-Triamino-2,4,6-trinitrobenzene (TATB) to Nuclear Quantum Effects. *Journal of Physical Chemistry C* **2019**, *123*, 21969–21981.

(26) Zeng, J.; Cao, L.; Xu, M.; Zhu, T.; Zhang, J. Z. Complex reaction processes in combustion unraveled by neural network-based molecular dynamics simulation. *Nature Communications* **2020**, *11*, 1–9.

(27) Yoo, P.; Sakano, M.; Desai, S.; Islam, M. M.; Liao, P.; Strachan, A. Neural network reactive force field for C, H, N, and O systems. *npj Computational Materials* **2021**, *7*, 1–10.

(28) Chu, Q.; Luo, K. H.; Chen, D. Exploring Complex Reaction Networks Using Neural Network-Based Molecular Dynamics Simulation. *Journal of Physical Chemistry Letters* **2022**, *13*, 4052–4057.

(29) Zhang, S.; Makoś, M. Z.; Jadrich, R. B.; Kraka, E.; Barros, K.; Nebgen, B. T.; Tretiak, S.; Isayev, O.; Lubbers, N.; Messerly, R. A.; Smith, J. S. Exploring the frontiers of condensed-phase chemistry with a general reactive machine learning potential. *Nature Chemistry* **2024**, *16*, 727–734.

(30) Lindsey, R. K.; Bastea, S.; Lyu, Y.; Hamel, S.; Goldman, N.; Fried, L. E. Chemical evolution in nitrogen shocked beyond the molecular stability limit. *Journal of Chemical Physics* **2023**, *159*, 84502.

(31) Zhang, J.; Guo, W.; Yao, Y. Deep Potential Molecular Dynamics Study of Chapman-Jouguet Detonation Events of Energetic Materials. *Journal of Physical Chemistry Letters* **2023**, *14*, 7141–7148.

(32) Lindsey, R. K.; Fried, L. E.; Goldman, N. ChIMES: A Force Matched Potential with Explicit Three-Body Interactions for Molten Carbon. *J. Chem. Theory Comput.* **2017**, *13*, 6222–6229.

(33) Ornellas, D. L. *Calorimetric Determinations of the Heat and Products of Detonation for Explosives: October 1961 to April 1982*; 1982.

(34) Christenson, J. G.; Fried, L. E.; Bastea, S.; Nielsen, M. H.; Willey, T. M.; Bagge-Hansen, M. The role of detonation condensates on the performance of 1,3,5-triamino-2,4,6-trinitrobenzene (TATB) detonation. *J. Appl. Phys.* **2022**, 095901.

(35) Tarver, C. M. Jones-Wilkins-Lee Unreacted and Reaction Product Equations of State for Overdriven Detonations in Octogen- and Triaminotrinitrobenzene-Based Plastic-Bonded Explosives. *J. Phys. Chem. A* **2020**, *124*, 1399–1408.

(36) Lindsey, R. K.; Fried, L. E.; Goldman, N. Application of the ChIMES Force Field to Nonreactive Molecular Systems: Water at Ambient Conditions. *J. Chem. Theory Comput.* **2019**, *15*, 436–447.

(37) Chen, M.; Ko, H. Y.; Remsing, R. C.; Andrade, M. F. C.; Santra, B.; Sun, Z.; Selloni, A.; Car, R.; Klein, M. L.; Perdew, J. P.; Wu, X. Ab initio theory and modeling of water. *Proceedings of the National Academy of Sciences of the United States of America* **2017**, *114*, 10846–10851.

(38) Si, Y.; Li, M.; Zhou, Z.; Liu, M.; Prezhdo, O. Improved description of hematite surfaces by the SCAN functional. *Journal of Chemical Physics* **2020**, *152*, 24706.

(39) Adamo, C.; Cossi, M.; Barone, V. An accurate density functional method for the study of magnetic properties: the PBE0 model. *Journal of Molecular Structure: THEOCHEM* **1999**, *493*, 145–157.

(40) Davidson, A. J.; Dias, R. P.; Dattelbaum, D. M.; Yoo, C.-S. "Stubborn" triaminotrinitrobenzene: Unusually high chemical stability of a molecular solid to 150 GPa. *The Journal of Chemical Physics* **2011**, *135*, 174507.

(41) Kroonblawd, M. P.; Fried, L. E. High Explosive Ignition through Chemically Activated Nanoscale Shear Bands. *Phys. Rev. Lett.* **2020**, *124*, 206002.

(42) Lindsey, R. K.; Fried, L. E.; Goldman, N.; Bastea, S. Active learning for robust, high-complexity reactive atomistic simulations. *The Journal of Chemical Physics* **2020**, *153*, 134117.

(43) Pham, C. H.; Lindsey, R. K.; Fried, L. E.; Goldman, N. High-Accuracy Semiempirical Quantum Models Based on a Minimal Training Set. *Journal of Physical Chemistry Letters* **2022**, *13*, 2934–2942.

(44) Smith, J. S.; Nebgen, B.; Lubbers, N.; Isayev, O.; Roitberg, A. E. Less is more: Sampling chemical space with active learning. *The Journal of Chemical Physics* **2018**, *148*, 241733.

(45) Lindsey, R. K.; Goldman, N.; Fried, L. E.; Bastea, S. Many-body reactive force field development for carbon condensation in C/O systems under extreme conditions. *The Journal of Chemical Physics* **2020**, *153*, 54103.

(46) Yates, L. A.; Aandahl, Z.; Richards, S. A.; Brook, B. W. Cross validation for model selection: A review with examples from ecology. *Ecological Monographs* **2023**, *93*, e1557.

(47) Tibshirani, R. Regression Shrinkage and Selection via the Lasso. *J. R. Statist. Soc. B* **1996**, *58*, 267–288.

(48) Efron, B.; Hastie, T.; Johnstone, I.; Tibshirani, R. Least Angle Regression. *The Annals of Statistics* **2004**, *32*, 407–499.

(49) E., H. A.; W., K. R. Ridge Regression: Biased Estimation for Nonorthogonal Problems. *Technometrics* **1970**, *12*, 55–67.

(50) Efthimiopoulos, I.; Stavrou, E.; Umemoto, K.; Mayanna, S.; Torode, A.; Smith, J. S.; Chariton, S.; Prakapenka, V. B.; Goncharov, A. F.; Wang, Y. High-pressure phase of cold-compressed bulk graphite and graphene nanoplatelets. *Physical Review B* **2023**, *107*, 184102.

(51) Occelli, F.; Loubeyre, P.; Letoullec, R. Properties of diamond under hydrostatic pressures up to 140 GPa. *Nature Materials* **2003**, *2*, 151–154.

(52) Stevens, L. L.; Velisavljevic, N.; Hooks, D. E.; Dattelbaum, D. M. Hydrostatic Compression Curve for Triamino-Trinitrobenzene Determined to 13.0 GPa with Powder X-Ray Diffraction. *Propellants, Explosives, Pyrotechnics* **2008**, *33*, 286–295.

(53) Stavrou, E.; Zaug, J. M.; Bastea, S.; Crowhurst, J. C. The equation of state of 5-nitro-2,4-dihydro-1,2,4,-triazol-3-one determined via in-situ optical microscopy and interferometry measurements. *Journal of Applied Physics* **2016**, *119*, 135904.

(54) Plisson, T.; Pineau, N.; Weck, G.; Bruneton, E.; Guignot, N.; Loubeyre, P. Equation of state of 1,3,5-triamino-2,4,6-trinitrobenzene up to 66 GPa. *Journal of Applied Physics* **2017**, *122*, 235901.

(55) Kroonblawd, M. P.; Lafourcade, P.; Fried, L. E.; Maillet, J. B.; Sewell, T. New Nonreactive Force Field for Accurate Molecular Dynamics Simulations of TATB at Extreme Conditions. *Journal of Chemical and Engineering Data* **2024**, *69*, 1526–1545.

(56) Koziol, L.; Fried, L. E.; Goldman, N. Using force matching to determine reactive force fields for water under extreme thermodynamic conditions. *Journal of Chemical Theory and Computation* **2017**, *13*, 135–146.

(57) Reed, E. J.; Fried, L. E.; Joannopoulos, J. A method for tractable dynamical studies of single and double shock compression. *Phys. Rev. Lett.* **2003**, *90*, 235503.

(58) Reed, E. J.; Fried, L. E.; Henshaw, W. D.; Tarver, C. M. Analysis of simulation technique for steady shock waves in materials with analytical equations of state. *Phys. Rev. E* **2006**, *74*, 056706.

(59) Plimpton, S. Fast parallel algorithms for short-range molecular dynamics. *J. Phys. Chem. C* **1995**, *117*, 1–19.

(60) Dobratz, B. M.; Crawford, P. C. *LLNL explosives handbook: properties of chemical explosives and explosives and explosive simulants*; 1985.

(61) Marshall, M. C.; Fernandez-Pañella, A.; Myers, T. W.; Eggert, J. H.; Erskine, D. J.; Bastea, S.; Fried, L. E.; Leininger, L. D. Shock Hugoniot measurements of single-crystal 1,3,5-triamino-2,4,6-trinitrobenzene (TATB) compressed to 83 GPa. *Journal of Applied Physics* **2020**, *127*, 185901.

(62) Sollier, A.; HC)bert, P.; Lescoute, E.; Lafourcade, P. Hugoniot measurements of the 1,3,5-triamino-2,4,6-trinitrobenzene (TATB) formulation T2 up to 70 GPa. *Journal of Applied Physics* **2024**, *135*, 95901.

(63) Zhang, L.; Zybin, S. V.; Duin, A. C. V.; Dasgupta, S.; Goddard, W. A.; Kober, E. M. Carbon cluster formation during thermal decomposition of octahydro-l,3,5,7-tetranitro-l,3,5,7-tetrazocine and l,3,5-triamino-2,4,6- trinitrobenzene high explosives from ReaxFF reactive molecular dynamics simulations. *Journal of Physical Chemistry A* **2009**, *113*, 10619–10640.

(64) Lindsey, R. K.; Goldman, N.; Fried, L. E.; Bastea, S. Chemistry-mediated Ostwald ripening in carbon-rich C/O systems at extreme conditions. *Nature Communications* **2022**, *13*, 1–7.

(65) Steele, B. A.; Perreault, C.; Baker, J.; Pham, H.; Crowhurst, J. Experimental and theoretical investigation into the high pressure deflagration products of 2,6-diamino-3,5-dinitropyrazine-1-oxide (LLM-105). *Combustion and Flame* **2025**, *275*, 114067.

(66) Batatia, I.; Benner, P.; Chiang, Y.; Elena, A. M.; Kovács, D. P.; Riebesell, J.; Advincula, X. R.; Asta, M.; Avaylon, M.; Baldwin, W. J.; Berger, F.; Bernstein, N.; Bhowmik, A.; Bigi, F.; Blau, S. M.; Cărare, V.; Ceriotti, M.; Chong, S.; Darby, J. P.; De, S.; Della Pia, F.; Deringer, V. L.; Elijošius, R.; El-Machachi, Z.; Fako, E.; Falcioni, F.; Ferrari, A. C.; Gardner, J. L. A.; Gawkowski, M. J.; Genreith-Schriever, A.;

George, J.; Goodall, R. E. A.; Grandel, J.; Grey, C. P.; Grigorev, P.; Han, S.; Handley, W.; Heenen, H. H.; Hermansson, K.; Ho, C. H.; Hofmann, S.; Holm, C.; Jaafar, J.; Jakob, K. S.; Jung, H.; Kapil, V.; Kaplan, A. D.; Karimitari, N.; Kermode, J. R.; Kourtis, P.; Kroupa, N.; Kullgren, J.; Kuner, M. C.; Kuryla, D.; Liepuoniute, G.; Lin, C.; Margraf, J. T.; Magdău, I.-B.; Michaelides, A.; Moore, J. H.; Naik, A. A.; Niblett, S. P.; Norwood, S. W.; O'Neill, N.; Ortner, C.; Persson, K. A.; Reuter, K.; Rosen, A. S.; Rosset, L. A. M.; Schaaf, L. L.; Schran, C.; Shi, B. X.; Sivonxay, E.; Stenczel, T. K.; Sutton, C.; Svahn, V.; Swinburne, T. D.; Tilly, J.; van der Oord, C.; Vargas, S.; Varga-Umbrich, E.; Vegge, T.; Vondrák, M.; Wang, Y.; Witt, W. C.; Wolf, T.; Zills, F.; Csányi, G. A foundation model for atomistic materials chemistry. *The Journal of Chemical Physics* **2025**, *163*, 184110.

(67) Becke, A. D. Density-functional exchange-energy approximation with correct asymptotic behavior. *Physical Review A* **1988**, *38*, 3098.

(68) Lee, C.; Yang, W.; Parr, R. G. Development of the Colle-Salvetti correlation-energy formula into a functional of the electron density. *Physical Review B* **1988**, *37*, 785.

(69) Grimme, S.; Antony, J.; Ehrlich, S.; Krieg, H. A consistent and accurate ab initio parametrization of density functional dispersion correction (DFT-D) for the 94 elements H-Pu. *Journal of Chemical Physics* **2010**, *132*, 154104.

(70) Grimme, S. Semiempirical GGA-type density functional constructed with a long-range dispersion correction. *Journal of Computational Chemistry* **2006**, *27*, 1787–1799.

(71) Winey, J. M.; Toyoda, Y.; Gupta, Y. M. Shock-induced chemical decomposition and overdriven detonation in hexahydro-1,3,5-trinitro-1,3,5-triazine (RDX) single crystals. *Journal of Applied Physics* **2022**, *132*, 95905.

(72) Hourahine, B.; Aradi, B.; Blum, V.; Bonafé, F.; Buccheri, A.; Camacho, C.; Cevallos, C.; Deshaye, M. Y.; Dumitrică, T.; Dominguez, A.; Ehlert, S.; Elstner, M.; van der

Heide, T.; Hermann, J.; Irle, S.; Kranz, J. J.; Köhler, C.; Kowalczyk, T.; Kubař, T.; Lee, I. S.; Lutsker, V.; Maurer, R. J.; Min, S. K.; Mitchell, I.; Negre, C.; Niehaus, T. A.; Niklasson, A. M. N.; Page, A. J.; Pecchia, A.; Penazzi, G.; Persson, M. P.; Řezáč, J.; Sánchez, C. G.; Sternberg, M.; Stöhr, M.; Stuckenberg, F.; Tkatchenko, A.; Yu, V. W.-z.; Frauenheim, T. DFTB+, a software package for efficient approximate density functional theory based atomistic simulations. *The Journal of Chemical Physics* **2020**, *152*, 124101.

(73) Gaus, M.; Goez, A.; Elstner, M. Parametrization and benchmark of DFTB3 for organic molecules. *Journal of Chemical Theory and Computation* **2013**, *9*, 338–354.

(74) Kresse, G.; Hafner, J. Ab initio molecular dynamics for liquid metals. *Physical Review B* **1993**, *47*, 558.

(75) Kresse, G.; Hafner, J. Ab initio molecular-dynamics simulation of the liquid-metal–amorphous-semiconductor transition in germanium. *Physical Review B* **1994**, *49*, 14251.

(76) Kresse, G.; Furthmüller, J. Efficiency of ab-initio total energy calculations for metals and semiconductors using a plane-wave basis set. *Computational Materials Science* **1996**, *6*, 15–50.

(77) Kresse, G.; Furthmüller, J. Efficient iterative schemes for ab initio total-energy calculations using a plane-wave basis set. *Physical Review B* **1996**, *54*, 11169.

(78) Blöchl, P. E. Projector augmented-wave method. *Physical Review B* **1994**, *50*, 17953.

(79) Kresse, G.; Joubert, D. From ultrasoft pseudopotentials to the projector augmented-wave method. *Physical Review B* **1999**, *59*, 1758.

(80) Perdew, J. P.; Burke, K.; Ernzerhof, M. Generalized Gradient Approximation Made Simple. *Physical Review Letters* **1996**, *77*, 3865.